NJC

PAPER

Cite this: *New J. Chem.*, 2017, **41**, 14659

The role of non-covalent interactions in some 2-trifluoromethylchromones in the solid state†

Christian David Alcívar León,[a] Gustavo Alberto Echeverría,[b] Oscar Enrique Piro,[b] Sonia Elizabeth Ulic, *[cd] Jorge Luis Jios, *[e] Jaime Andrés Pereañez,[f] Isabel Cristina Henao Castañeda[g] and Hiram Pérez[h]

Received 9th February 2017,
Accepted 25th October 2017

DOI: 10.1039/c7nj00481h

rsc.li/njc

The intermolecular interactions in the solid state and the spectroscopic vibrational, electronic and NMR properties of new 3-methyl-substituted-2-trifluoromethylchromone derivatives with –CN (**1**), $-NO_2$ (**2**), –OH (**3**) and $-NH_2$ (**4**) groups were discussed with the assistance of DFT calculations. The crystal structures of compounds **1–3** were determined by X-ray diffraction showing molecular ribbons for compounds **1** and **2**, and dimers *via* O–H···O=C hydrogen bonds for **3**. Hirshfeld surfaces and the corresponding fingerprint plots, as well as the electrostatic potentials mapped on the surfaces revealed C–H···O and C–H···F hydrogen bonds, and π···π stacking as the main cooperative driving forces for building supramolecular architectures in all compounds. The C–H···π and C=O···π interactions also contribute to stabilizing the crystal structures of **1** and **2**. A further analysis of Hirshfeld surfaces was performed using the enrichment ratio as a new descriptor to determine the likelihood of chemical species to establish specific interactions in the molecular packing. The lattice energies of the crystal structures and several intermolecular contacts present in different molecular pairs were also quantified. Molecular docking studies showed the interaction of the title compounds with the catalytic site of PLA_2 (PDB code 2QOG) from *Crotalus durissus terrificus*, and suggested that the investigated compounds could inhibit toxic effects of snake venom.

[a] *Centro de Investigación de Alimentos, CIAL, Facultad de Ciencias de la Ingeniería e Industrias, Universidad Tecnológica Equinoccial, EC171029 Quito, Ecuador*
[b] *Departamento de Física, Facultad de Ciencias Exactas, Universidad Nacional de La Plata e IFLP (CONICET, CCT-La Plata), C. C. 67, (1900) La Plata, Republica Argentina*
[c] *CEQUINOR (CONICET-UNLP), Facultad de Ciencias Exactas, Universidad Nacional de La Plata, Bv. 120 e/60 y 64 No. 1465 (1900), La Plata, Republica Argentina. E-mail: sonia@quimica.unlp.edu.ar*
[d] *Departamento de Ciencias Básicas, Universidad Nacional de Luján, Rutas 5 y 7, (6700) Luján, Buenos Aires, Republica Argentina*
[e] *UNIDAD PLAPIMU-LASEISIC (UNLP-CIC), Departamento de Química, Facultad de Ciencias Exactas, Universidad Nacional de La Plata, Camino Centenario e/505 y 508, (1897) Gonnet, Republica Argentina. E-mail: jljios@quimica.unlp.edu.ar*
[f] *Programa de Ofidismo/Escorpionimo, Facultad de Ciencias Farmacéuticas y Alimentarias, Universidad de Antioquia UdeA, Calle 70 No. 52-21, Medellín, Colombia*
[g] *Grupo de Productos Naturales Marinos, Facultad de Ciencias Farmacéuticas y Alimentarias, Universidad de Antioquia UdeA, Calle 70 No. 52-21, Medellín, Colombia*
[h] *Departamento de Química Inorgánica, Facultad de Química, Universidad de La Habana, La Habana 10400, Cuba*

† Electronic supplementary information (ESI) available: Experimental details and spectroscopic characterization of compounds **1–4**. A view of the molecular structure of compounds **1–3** showing the atom-numbering scheme with displacement ellipsoids at the 30% probability level (Fig. S1–S3). A view of the hydrogen-bonding interactions (dashed lines) for compounds **5** and **6** (Fig. S4 and S5). Hirshfeld surfaces mapped with electrostatic potential (ESP) showing selected electropositive and electronegative potentials (a.u.) (Fig. S6). A view of the π···π stacking and C=O···π (dashed lines) interactions showing intercentroid and O···Cg1 distances for compound **5** (Fig. S7). A view of the π–π stacking (dashed lines) interactions showing intercentroid distances for compound **6** (Fig. S8). Views of the Hirshfeld surfaces in two orientations for compounds **5** and **6** (Fig. S9). Hirshfeld surfaces mapped with *shape index* and *curvedness* for compounds **5** and **6** (Fig. S10). Fingerprint plots of compounds **5** and **6** (Fig. S11). Potential energy curve for the torsional angle around ϕ(CC-CCH_2R) of **1–4**, calculated at the B3LYP/6-311++G(d,p) level of theory (Fig. S12a–d). Infrared and Raman spectra of solid **1–4** at room temperature (Fig. S13a–d). Experimental (full trace, in methanol) and calculated electronic spectra (CPCM/B3LYP/6-311++G(d,p), dashed and full trace) for compounds **1–4** (Fig. S14). Molecular orbitals involved in the electronic transitions of **1–4** (Fig. S15–S18). Comparison of experimental and theoretical chemical shifts of **1–4** for ^{1}H and ^{13}C (Fig. S19). (a) ^{1}H and (b) ^{13}C NMR spectra of **1–4** (Fig. S20–S23). Docking results between compounds and a snake venom PLA_2 for compound **1** and **2** (Fig. S24a and b). Selected experimental (X-ray diffraction) and calculated (B3LYP/6-311++g(d,p)) bond lengths [Å], bond angles [°], and torsion angles [°] [a] of **1–3** (Table S1). Bond lengths [Å] and angles [°] in **1–3** (Tables S2–S4). Atomic coordinates ($\times 10^4$) and equivalent isotropic displacement parameters (Å^2 × 10^3) for **1–3** (Tables S5–S7). Anisotropic displacement parameters for **1–3** (Tables S8–S10). Hydrogen coordinates and isotropic displacement parameters for **1–3** (Tables S11–S13). Lattice energies (kJ mol^{-1}) partitioned into coulombic (E_{coul}), polarization (E_{pol}), dispersion (E_{disp}) and repulsion (E_{rep}) components for **1–3**, **5** and **6** (Table S14). Geometrical parameters for the π-stacking moieties involved in the π···π interactions for compounds **1–3**, **5** and **6** (Å, °) (Table S15). Hirshfeld contact surfaces C_{XY}(%)*, proportion of chemical type on the molecular surface S_X (%) and random contacts R_{XY}(%) of the main intermolecular contacts for compounds **1–3**, **5** and **6** (Table S16). Enrichment ratios E_{XY} of the main intermolecular contacts for compounds **1–3**, **5** and **6** (Table S17). Experimental and calculated frequencies (cm^{-1}) and tentative fundamental vibration mode assignment of **1–4** (Tables S18–S21). CCDC 1473665–1473667. For ESI and crystallographic data in CIF or other electronic format see DOI: 10.1039/c7nj00481h

1. Introduction

The title compounds belong to the family of chromones, a well known class of heterocyclic skeleton that is habitual in natural products, especially in plants,[1] and in pharmaceutical agents and drugs. The potential biological significance of chromones has been reviewed in the last few years,[2,3] showing that they exhibit good anti-inflammatory,[4] antimicrobial,[5,6] antiviral,[7] anti-HIV,[8] and anticancer activity.[9–11]

The rational drug design and development of materials with improved physicochemical properties such as lipophilicity (bioavailability) has led to new synthetic methods for introducing halogen atoms, especially the lighter fluorine and chlorine atoms, since they are substituents widely used in medicinal chemistry.[12–14] In addition, the interchange of hydrogen by fluorine is one of the most commonly employed monovalent isosteric replacements.[15] Therefore, the influence of the electron-withdrawing effect caused by fluorine substitution is relevant for the interaction either with a biological receptor or enzyme, as well as for the metabolic stability.[15] In this sense, molecular docking is an interesting approach for the identification of bioactive molecules.[16,17] Compared with traditional experimental high-throughput screening (HTS), *in silico* virtual screening methodology is a more direct and rational drug discovery approach, since it allows the identification of non-binding compounds. This advantage lies in the low cost and effective screening,[16] with the number of compounds that need to be tested *in vitro* being dramatically reduced, sometimes by orders of magnitude.[17] Pathophysiological effects observed in envenomations by snake bites combine the action of several enzymes, proteins and peptides. Phospholipases A_2 (PLA_2) that abundantly occur in snake venoms are calcium dependent enzymes that hydrolyze glicerophospholipids inducing systemic and local myotoxicity, myonecrosis, neurotoxicity and hemolytic activity, among others.[18–20] The hydrophobic channel of this enzyme leads the substrate to the active site, which is responsible for coordinating the Ca^{2+} required during catalysis.[21]

In addition, halogens as substituents enable halogen bonding interactions in the host molecule, which is considered as highly-directional non-covalent interaction[22] of weak to medium intensity, that can compete or act synergistically with weak to moderately strong hydrogen bonds. The role of such interaction in drug discovery was recently reviewed.[13] Besides, non-covalent interactions play an essential role in supramolecular chemistry, molecular biology and crystal engineering.[22–25] Various attempts have been made to elucidate and quantify them, including non-classical hydrogen bonding,[26,27] π···π stacking,[28,29] C–H···π[30] and C=O···π[31] interactions. All these interactions can be quantified by Hirshfeld surface analysis[29,32,33] based on tools such as d_{norm}, shape index and curvedness surface properties and the fingerprint plots[32,34] display a quantitative picture of intermolecular contacts. Recently, a discussion about the role of intermolecular bonds (and their strength) was published in order to describe, interpret, predict and control the crystal structure and other processes.[35]

The C–H···F interactions have been controversial in the literature. It has been reported that fluorine does not easily form hydrogen bonding in an organic environment,[36] but recently it was found that the presence of a fluorine atom modifies the crystal packing in certain systems. Thus, structural studies in fluorobenzenes revealed the presence of supramolecular motifs based on C–H···F interactions, similar to C–H···O and C–H···N hydrogen bonds.[37,38] It has also been described that C–H···O and C–H···F interactions are not purely electrostatic.[39]

As is known, the C–F organic fluorine is a poor hydrogen-bond acceptor, especially in systems where O–H/N–H···F–C hydrogen bonds are in competition. However, the C–H group acts as a hydrogen-bond donor, so increasing the relative proportion of fluorine atoms enhances the acidity of the C–H group,[40] and therefore weak C–H···F interactions may be distinguished. It is important to highlight that in the absence of strong hydrogen bonds, fluorine has the ability to form different supramolecular motifs such as dimers, chains, chains of dimers, tetramers, *etc.* *via* C–H···F–C contacts.[41,42]

Some authors[42] have performed statistical analysis in data sets of crystal structures retrieved from CSD, focusing on the study of intermolecular contacts shorter than the sum of van der Waals radii. They found that the lattice energies of the structures are dominated by dispersion, with the frequency of C–H···F contacts being sparse or just sporadic, and the intermolecular interaction energies are not usually dominated by C–H···X coulombic components. Recently, Taylor[47] used a new parameter R_F to evaluate the occurrence of C–H···F hydrogen bond interactions (RF = 1 is the expected value if packing was random). Surprisingly, the F···H interactions exhibit the highest R_F of 3.5 indicating that they occur 3.5 times more often than would be expected from surface area considerations. Although C–H···O and C–H···N are energetically stronger than C–H···F interactions, the last contact is of great significance in stabilizing crystal packing even when the distance is longer than the sum of vdW radii.

In this work the graph-set motifs of intermolecular networks were assigned together with the analysis of intermolecular hydrogen bonding, π–aromatic interactions and other weak non-covalent intermolecular contacts. They were based on the X-ray structures of new 2-trifluoromethyl-3-CH_2R substituted chromones (R: –CN (**1**), $–NO_2$ (**2**), –OH (**3**)) and two related ones (R: –H (**5**), –Br (**6**)).[43] The role of such interactions was expanded to the study of **1–4** binding with the catalytic site of phospholipase A_2 (PLA_2). Additionally, the NMR (^{1}H, ^{13}C, ^{19}F), UV-Vis and vibrational (IR and Raman) spectra were assigned with the assistance of theoretical calculations. In spite of other methodologies,[44–46] the one pot synthesis of 2-trifluoromethylchromones[47] was used to obtain four new 3-methyl derivatives **1–4** (see Scheme 1).

2. Experimental

2.1. Instrumentation

Infrared and Raman spectroscopy. Infrared absorption spectra (KBr pellets) were recorded on a LUMEX InfraLUM FT-02

spectrometer with a resolution of 2 cm^{-1} in the range from 4000 to 400 cm^{-1}. Solid Raman dispersion spectra at room temperature were obtained using a Thermoscientific DXR Raman microscope (spectral resolution 4 cm^{-1}). The 532 nm radiation line of a diode-pump solid state laser was used for excitation in the 3500–100 cm^{-1} spectral range.

NMR spectra. The ^{1}H (500.0 MHz), ^{19}F (471 MHz) and ^{13}C (125.7 MHz) NMR spectra were recorded at 25 °C on a Bruker Avance II 500 spectrometer. The samples were dissolved in $CDCl_3$ and the solution was introduced into a 5 mm NMR tube. Chemical shifts (δ) are given in parts per million (ppm) relative to tetramethylsilane (TMS, δ = 0 ppm). For the ^{19}F NMR spectrum, a 0.05% TFA in $CDCl_3$ solution was used as an external reference (δ = −71.0 ppm). Coupling constants (J) are reported in Hz, with singlets being indicated as s, doublets as d, double doublets as dd, double double doublets as ddd, triplets as t, quartets as q, broad singlets as br.s and broad doublets as br.d. For NMR data, the standard numbering scheme of the benzopyrane skeleton (with the bridged oxygen atom carrying the number 1) was adopted to facilitate the comparison with data reported in the literature (see Scheme 1).

UV-Visible spectroscopy. The spectra were recorded in methanol using a quartz cell (10 mm optical path length) on a ChromTech CT-5700 UV/Vis spectrophotometer at 2.0 nm spectral bandwidth. Measurements were carried out in the spectral region from 190 to 1100 nm.

Mass spectrometry. The MS determinations were performed by injection of methanol solutions (~1 μl) in a HP 5890 Chromatograph coupled to a HP 5972 A mass selective detector. An HP5-MS capillary column (30 m × 0.25 mm × 5 μm) has been used with H_2 as the carrier gas (0.6 ml min^{-1}). The temperature set points were: 200 °C in the split injector, 300 °C in the interface, 185 °C in the ion source and the oven ramp started at 80 °C and ended at 200 °C with a heating rate of 10 °C min^{-1}. The electron energy was 70 eV with a mass range of 50–350 amu and a pressure in the mass spectrometer lower than 10^{-5} Torr. The compounds **2** and **3** were analyzed by direct insertion probe-mass spectrometry with electron ionization (DIP-EI-MS).

X-ray diffraction data. The measurements were performed on an Oxford Xcalibur, Eos, Gemini CCD diffractometer with graphite-monochromated CuKα (λ = 1.54184 Å) radiation. X-ray diffraction intensities were collected (ω scans with θ and κ-offsets), integrated and scaled with the CrysAlisPro[48] suite of programs. The unit cell parameters were obtained by least-squares refinement (based on the angular settings for all collected reflections with intensities larger than seven times the standard deviation of measurement errors) using CrysAlisPro. Data were corrected empirically for absorption employing the multi-scan method implemented in CrysAlisPro. The structures were solved by direct methods with SHELXS[49] of the SHELX suite of programs. The molecular models were refined by the full-matrix least-squares procedure with SHELXL[50] of the same package. The trifluoromethyl group of **3** showed severe rotational disorder around the C–CF_3 bond which could be modeled in terms of four angularly split replicas. These were refined with isotropic displacement parameters for the fluorine atoms and restraining the C–F bond lengths and F···F distances to be, respectively, equal to one another while keeping the sum of the occupancies equal to one. All H-atoms of **1** and **3** were located in a Fourier difference map and refined at their found positions while the ones of **2** were refined with the riding model. Crystal data, data collection procedure, and refinement results for all three complexes are summarized in Table 1. Ortep[51] and Mercury[52] programs were used for molecular graphics. The geometric parameters of π-stacking interactions were computed with PLATON for Windows Taskbar v1.17.[53] Crystallographic structural data have been deposited at the Cambridge Crystallographic Data Centre (CCDC). CCDC 1473665 (**1**), 1473666 (**2**), and 1473667 (**3**).†

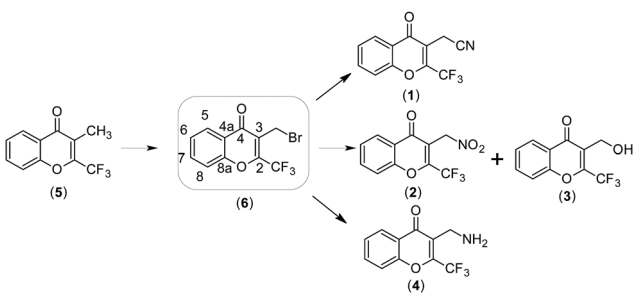

Scheme 1 New methyl-derivatives **1–4**, from 3-bromomethyl-2-trifluoromethylchromone **6**.

2.2. Synthesis

The title compounds 3-cyanomethyl-2-trifluoromethylchromone (**1**),[54] 3-nitromethyl-2-trifluoromethylchromone (**2**)[55] and 3-hydroxymethyl-2-trifluoromethylchromone (**3**) were obtained following reported procedures with slight modifications whereas 3-aminomethyl-2-trifluoromethylchromone (**4**) was synthesized using ammonia gas as a nucleophilic agent.[56] The experimental details and spectroscopic characterization are described in the ESI.†

2.3. Computational methods

Quantum chemical methods for compounds **1–4** were performed for calculating vibrational frequencies (IR, Raman), UV-Vis transitions, NMR chemical shifts (^{1}H, ^{13}C) and molecular docking, using the Gaussian 09 program package.[57] The relaxed potential energy surface scans, geometry optimizations and vibrational frequency calculations were carried out with the Density Functional Theory (B3LYP) method employing the 6-311++G(d,p) basis set. NBO calculations at the B3LYP/6-31G(d,p) level were performed to investigate the relative strength of all hydrogen bonds (intra and intermolecular).

In all cases, the calculated vibrational properties correspond to potential energy minima with no imaginary values for the frequencies, which indicates that each optimized structure corresponds to a real minimum on the potential energy surfaces. Then, the most stable conformers computed for **1–4** were used as ligands in molecular docking studies. The ^{1}H and ^{13}C chemical shifts were calculated with B3LYP/6-311+g(2d,p) optimized geometries by the GIAO method (Gauge Including Atomic Orbital), using the corresponding TMS shielding calculated at

Table 1 Crystal data and structure refinement results for **1–3**

Compound	**1**	**2**	**3**
Empirical formula	$C_{12}H_6F_3NO_2$	$C_{11}H_6F_3NO_4$	$C_{11}H_7F_3O_3$
Formula weight	253.18	273.17	244.17
Temperature (K)	297(2)	297(2)	297(2)
Crystal system	Monoclinic	Monoclinic	Monoclinic
Space group	$P2_1/c$	$P2_1/a$	$P2_1/n$
Unit cell dimensions			
a (Å)	7.6164(8)	7.5438(5)	4.7865(2)
b (Å)	19.798(2)	20.212(1)	15.3885(6)
c (Å)	7.849(1)	7.7385(6)	13.7073(5)
β (°)	114.01(1)	110.717(9)	93.722(3)
Volume (Å^3)	1081.2(2)	1103.6(1)	1007.51(7)
Z, density (calc., Mg m^{-3})	4, 1.555	4, 1.644	4, 1.610
Absorpt. coeff. (mm^{-1})	1.242	1.405	1.350
F(000)	512	552	496
Crystal size (mm^3)	0.662 × 0.387 × 0.084	0.485 × 0.214 × 0.125	0.511 × 0.120 × 0.084
θ-Range (°) for data collection	4.325 to 72.418	4.467 to 73.491	4.375 to 70.959
Index ranges	$-9 \le h \le 8$, $-24 \le k \le 17$, $-9 \le l \le 7$	$-9 \le h \le 7$, $-23 \le k \le 24$, $-9 \le l \le 9$	$-4 \le h \le 5$, $-16 \le k \le 18$, $-16 \le l \le 14$
Reflections collected	4180	4195	6524
Independent reflections	[R(int) = 0.0222]	1648 [R(int) = 0.0278]	2815 [R(int) = 0.0199]
Completeness (%)	100.0 (to θ = 67.684°)	98.5 (to θ = 67.684°)	100.0 (to θ = 67.684°)
Data/restraints/parameters	2142/0/187	2092/0/173	1959/103/207
Goodness-of-fit on F^2	1.040	1.133	1.066
Final R indices [$I > 2\sigma(I)$]	R_1 = 0.0456, wR_2 = 0.1257	R_1 = 0.0757, wR_2 = 0.2382	R_1 = 0.0609, wR_2 = 0.1670
R indices (all data)	R_1 = 0.0629, wR_2 = 0.1447	R_1 = 0.1144, wR_2 = 0.3330	R_1 = 0.0677, wR_2 = 0.1758
Larg. diff. peak & hole (e Å^{-3})	0.142 and −0.222	0.301 and −0.390	0.248 and −0.392

the same level of theory.[58] Moreover, the theoretical electronic spectra were simulated with TD-DFT, taking into account implicitly the solvent effect (methanol).

2.4. Adopted criteria for interaction distances

The distance criteria[59] for crystal packing analysis of supramolecular motifs with cut-offs of 0.4 Å larger than the van der Waals (henceforth, vdW) radius[60] were adopted. Though it is generally accepted[61] that the directionality in a hydrogen bond must be at least 90°, we have considered a lower limit of 120°. Despite the geometric criteria for the existence of hydrogen bonds in solids considering only estimated vdW radii[42] being controversial, several authors have detected and determined certain interactions as ''hydrogen bonds'' by regarding exclusively geometric parameters. On the other hand, most influential distances on the crystal packing are missed when only distances at or below the vdW radii are considered.[62]

2.5. Lattice and interaction energies

Lattice and intermolecular interaction energies were calculated using the CLP (Coulomb–London–Pauli) approach implemented in the PIXEL program package,[63–65] which enables partitioning of the total energy into their coulombic, polarization, dispersion and repulsion contributions.

2.6. Hirshfeld surface calculations

Hirshfeld surfaces and their associated two-dimensional fingerprint plots[23,32,33] are obtained using CrystalExplorer3.1 software.[66] The d_{norm} (normalized contact distance) surface and the breakdown of two-dimensional fingerprint plots are used for decoding and quantifying intermolecular interactions in the crystal lattice. The d_{norm} is a symmetric function of distances to the surface from nuclei inside and outside the Hirshfeld surface (d_i and d_e, respectively), relative to their respective van der Waals radii. 3D d_{norm} surfaces are mapped over a fixed color scale of −0.243 a.u. (red)−0.824 Å a.u. (blue), shape index mapped in the color range of −1.0 a.u. (concave)−1.0 a.u. (convex) Å, and *Curvedness* in the range of −4.0 a.u. (flat)−0.4 a.u. (singular) Å. Hirshfeld surface properties are generally used to identify planar stacking arrangements.[33] The 2D fingerprint plots are displayed by using the translated 0.6–2.6 Å range, including reciprocal contacts. Electrostatic potentials on 0.008 e Å^3 isosurfaces were calculated at the Hartree–Fock level and with the 6-31g+ basis set using the Tonto program[67] integrated into CrystalExplorer.

2.7. Molecular docking

The more stable conformers of the ligands (**1–4**) were obtained from geometry optimizations using B3LYP/6-311++G(d,p) approximation as described in Computational methods (Section 2.3.) and they were transformed to the pdqt format file using Gauss View 5.[68] The phospholipase A2 (PLA2) structure from *Crotalus durissus terrificus* was downloaded from the Protein Data Bank (PDB code 2QOG) and the structure was prepared using the Protein Preparation module implemented in the Maestro program. In the first step water molecules were removed, and hydrogen atoms were automatically added to the protein according to the chemical nature of each amino acid on the basis of the ionized form expected under physiological conditions. This module also controls the atomic charges assignment. Then, the 3D structure of the protein was relaxed through constrained local minimization, using the OPLS (Optimized Potentials for Liquid Simulations) force field in order to remove possible structural mismatches due to the automatic procedure employed to add the hydrogen atoms. Bonds, bond orders, hybridizations, and hydrogen

atoms were checked and added when necessary; and a formal charge of +2 for Ca ions was assigned.

To setup the docking, the α-carbon of His48 was selected as a grid center, because it is the most important residue for the catalytic mechanism of the PLA2s. (Grid center coordinates X = 44.981, Y = 27.889; Z = 46.392, size 24 Å^3. Exhaustiveness = 20.) Additionally, the side chains of the PLA2 were kept rigid during the study, but ligands were considered as flexible depending on the rotatable bonds. Using prepared protein and ligand structures, molecular docking was carried out on a personal computer using Autodock Vina.[69] Although the program gave 10 possible poses with different affinity energies and orientations for each ligand, only those with best affinity were chosen. A visual inspection of the interactions at the active site was performed and recorded with Molegro Molecular Viewer (MMV 2.5.0, http://www.clcbio.com/products/molegro/#molecular-viewer) and UCSF Chimera (www.cgl.ucsf.edu/chimera/) was used to generate docking images. The final configurations of the compounds (**1–4**) in the PLA2 binding pocket were re-optimized at the B3LYP/6-311++G(d,p) level of theory in order to prove that structures still exist.

3. Results and discussion

3.1. Intra- and intermolecular interactions in the crystal structures

ORTEP[51] drawings of **1–3** and their main bond distances and angles near the methyl functional group are shown in Fig. S1–S3 and Table S1 (ESI†), respectively (see the complete bond lengths, angles and other crystallographic information in Tables S2–S13, ESI†). Attempts to obtain suitable crystals for X-ray diffraction measurement of **4** (–NH_2) were unsuccessful. Due to extended π-bonding, the chromone molecular skeleton in all three substances is planar (rms deviation of non-H atoms from the corresponding best least-squares planes is less than 0.05 Å) and, as expected, are nearly identical with one another. In fact, the rms separation between homologous non-H atoms in the best least-squares structural fitting of the solid state molecules, calculated by the Kabsh's procedure,[70] is less than or equal to 0.036 Å. Observed bond distances and angles agree with what is predicted by organic chemistry rules. In fact, for the better refined compound **1**, the phenyl ring C–C distances [from 1.369(3) to 1.405(3) Å] are consistent with a resonant-bond structure. The fused heterocycle shows a C6–C7 bond length of 1.339(3) Å, shorter than the other heterocycle C–C distances [1.465(3) and 1.468(3) Å], which corresponds to double bond character for that link. The C–O single bond distances are 1.345(2) and 1.381(2) Å, and the carbonyl C═O double bond length is equal to 1.222(3) Å. The –C(sp^3)F_3 group exhibits the expected carbon tetrahedral bonding structure with C–C–F angles from 111.0(2) to 112.5(2)° and F–C–F angles in the 106.9(2)–107.4(2)° range. Observed C–F bond distances are in the 1.322(3)–1.324(3) Å interval. The –CF_3 group in both compounds **1** and **2** adopts a staggered angular conformation. In **1**, the (CH_2)–CN bond distance is 1.463(3) Å and cyanide d(C–N) = 1.134(3) Å. In **2**, the (CH_2)–NO_2 distance is 1.515(6) Å and the N–O bond lengths are 1.206(5) and 1.215(5) Å with ∠(O–N–O) = 123.6(5)°. In **3**, the (CH_2)–OH distance is 1.407(3) Å.

The geometry of relevant intermolecular hydrogen bonds for structures **1–3** and two related structures,[43] labelled here as **5** (–CH_3) and **6** (–CH_2Br), are shown in Table 2 (column 4). In all five structures, C–H···O interactions are shorter than the sum of the vdW radii (2.72 Å) displaying H···O distances between 2.470 and 2.711 Å, so they satisfy the distance criteria defining C–H···O hydrogen bonds.[71] In addition, such interactions present notable directionality with angles in the range of 143–162°. It is well known that these weak interactions control crystal packing particularly in the absence of stronger hydrogen bonds.[72] They occur in the studied structures due to the presence of carbonyl and nitro (in **2**) groups as stronger C–H···O hydrogen bond acceptors.

Another key feature in the assembly of these structures is the existence of C–H···F hydrogen bonds. The sum of the vdW radii of hydrogen and fluorine has been assumed[62] as approximately 2.67 Å, and H···F interactions have been examined up to 3.0 Å, according to the described distance criteria.[59] In the analyzed structures, C–H···F hydrogen bonds adopt angle values in the range of 122–139°, indicating moderate angular directionality. For structure **5** values of 155 and 172° were also observed showing nearly linear C–H···F hydrogen bonds. This unusual feature has been reported in the literature, and such interactions in crystal structures with organic fluorine[73] have been classified as "extremely rare".

In the studied crystals, these weak intermolecular contacts build different structural motifs through a combination of C–H···O and C–H···F hydrogen bonds together with C–H···N in **1**, and O–H···O in **3** (see Table 2). Since **1** and **2** have no strong hydrogen bond donors, C–H···O (involving a benzene ring carbon and a carbonyl oxygen atom) and C–H···F (connecting a methylene group and a fluorine atom) hydrogen bonds are formed. These weak intermolecular contacts develop infinite chains which can be described as a C(6) first level graph-set. They are combined into a $R_2^2(12)$ second level graph-set building ribbons along the b-axis in **1** and the a-axis in **2**. Compound **3** also has an additional hydroxyl group and its molecules form dimers connected through strong O–H···O hydrogen bonds. Interestingly, the structure is dominated by O–H···O interactions instead of the weak C–H···O and C–H···F hydrogen bonds as observed in **1** and **2**. The resulting structural motif can be classified by the first level graph-set descriptor $R_2^2(12)$. In **1**, ribbons connect to each other by weak C–H···F hydrogen bonds, building (001) layers of an $R_2^2(12)R_5^4(20)$ second level graph-set (see Fig. 1). Furthermore, H···N distances of 2.54(3) and 2.75(3) Å are shorter and equal to the sum of the van der Waals radii (2.75 Å), respectively, and together with angles of 153° and 124° provide crystallographic evidence for the existence of C–H···N hydrogen bonds, as reported in the literature.[37] Therefore, the (001) layer packing of **1** might be assisted by a C–H···N hydrogen bond linking a C–H benzene ring with the cyanide nitrogen atom as well as π···π and van der Waals intermolecular interactions. The distances between mean chromone

Table 2 Interaction distances (Å), angles (°), (E_{TOT}) partitioned into coulombic, polarization, dispersion and repulsion contributions (kJ mol^{-1}) and (E_{MP2}) energies for different molecular pairs in **1–3**, **5** and **6**

Compound	Symmetry	Involved interactions	d(H···A), ∠D—H···A	Centroid distance	E_{coul}	E_{pol}	E_{disp}	E_{rep}	E_{TOT}	E_{MP2}[b]
1	$1+x, y, z$	C9–H9···O2	2.539(1), 162	7.616	−10.4	−4.1	−12.3	11.8	−15.1	−11.3
		C11–H11B···F3	2.69(3), 123							
	$1-x, \frac{1}{2}+y, 1.5-z$	C1–H1···F2	2.78(3), 139	10.562	−1.3	−0.4	−4.2	1.3	−4.7	−3.5
	$x, \frac{1}{2}-y, -\frac{1}{2}+z$	C11–H11A···N	2.54(3), 153	8.165	−7.9	−3.6	−9.9	9.2	−12.3	−8.2
	$-x, 1-y, 2-z$	C3–H3···N	2.75(3), 124	7.525	−18.7	−5.4	−18.0	12.2	−29.8	−25.4
	$-x, 1-y, 1-z$	H11B···Cg2, O2···Cg1	3.448(2)[a]	4.676	−13.3	−5.8	−43.4	27.2	−35.4	−34.8
	$1-x, 1-y, 2-z$	Cg···Cg	3.489(2)[a]	5.433	−16.8	−5.3	−42.3	22.2	−42.3	−37.9
2	$1-x, 1-y, -z$	C3–H3···O3	2.58(3), 146	7.101	−14.7	−4.0	−21.7	12.8	−27.7	−24.4
	$1-x, 1-y, 1-z$	C1–H1···O3, Cg···Cg	2.614(3), 149	6.071	−19.4	−5.8	−40.5	25.6	−40.1	−36.9
	$-\frac{1}{2}+x, 1.5-y, z$	C2–H2···O4	2.71(1), 123	7.790	−4.0	−2.0	−10.5	5.5	−11.1	−6.1
	$-x, 1-y, -z$	C3–H3···F1, Cg1···Cg1	2.993(4), 122	4.866	−13.4	−5.5	−44.1	25.5	−37.5	−36.5
		H11B···Cg2, O2···Cg1	—							
	$x, y, -1+z$	C11–H11B···F3	2.76(1), 131	7.739	−7.3	−2.9	−10.4	7.8	−12.7	−9.7
		C9–H9···O2	2.56(3), 165							
3	$-x, -y, 1-z$	O3–H···O2	1.92(5), 163	7.323	−71.9	−26.8	−24.8	73.6	−49.9	−36.7
	$-\frac{1}{2}-x, \frac{1}{2}+y, 1.5-z$	C1–H1···O3	2.470(1), 151	8.623	−9.1	−3.5	−11.4	10.6	−13.4	−9.7
		C1–H1···F2A	2.83(5), 124							
	$1+x, y, z$	Cg1···Cg2, F3A···Cg1	3.494(2)[a]	4.787	−5.8	−2.5	−37.3	21.2	−24.4	−22.7
	$-1+x, y, z$	Cg2···Cg1	3.494(2)[a]	4.787	−5.8	−2.5	−37.3	21.2	−24.4	−22.7
5	$1-x, -y, 2-z$	Cg···Cg	—	4.365	−12.4	−3.5	−46.9	31.0	−31.9	−31.5
	$1-x, -\frac{1}{2}+y, 1.5-z$	C3–H3···F3, O2···Cg1	2.64(3), 172	5.822	−11.5	−5.2	−23.3	19.0	−20.9	−16.3
	$x, \frac{1}{2}-y, -\frac{1}{2}+z$	C9–H9···O2	2.46(2), 154	6.308	−10.0	−3.3	−16.1	12.4	−17.0	−12.4
		C11–H11C···F2	2.81(2), 124							
	$1+x, \frac{1}{2}-y, \frac{1}{2}+z$	C1–H1···F1	2.81(2), 155	10.180	−1.9	−0.6	−7.2	2.7	−7.0	−4.1
		C2–H2···F3	2.79(2), 126							
6	$1+x, y, z$	C9–H9···O2	2.613(1), 143	7.462	−5.8	−2.9	−12.2	8.4	−12.5	−9.2
		C11–H11B···F1A	2.58(2), 138							
	$-x, 1-y, 1-z$	C1–H1···Br1, Cg···Cg	3.148(1), 147	6.261	−18.5	−4.3	−45.2	27.2	−40.8	−36.0

[a] Interplanar chromone distance of nearest neighbour molecules. [b] MP2/6-31G(d,p).

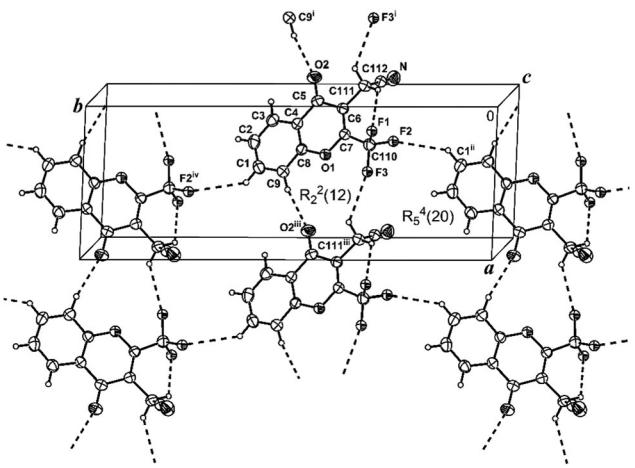

Fig. 1 C–H···O and C–H···F hydrogen bonds (dashed lines) for **1** showing the $R_2^2(12)$ and $R_4^5(20)$ graph-set motifs, the atom labeling and their displacement ellipsoids at the 30% probability level. Symmetries operations: (i) $-1+x, y, z$; (ii) $1-x, -1/2+y, 3/2-z$; (iii) $1+x, y, z$; (iv) $1/2-x, 1/2+y, 3/2-z$.

planes of nearest neighbour molecules are 3.448(2) and 3.489(2) Å (see Table 2). Similar weak hydrogen bonds were found in compounds **5** and **6** bearing 3-methyl and 3-bromomethyl substituents, respectively (Fig. S4 and S5, ESI†). In **2**, ribbons are linked by C–H···O contacts involving a C–H phenyl ring with an oxygen acceptor of the nitro group, building (100) layers of an $R_2^2(12)R_5^5(20)$ second level graph-set. Additionally, layers are stacked by C–H···O interactions between other C–H aromatic and nitro oxygen acceptor atoms. In **3**, the dimer is formed by molecules connected by two O–H···O hydrogen bonds, originating a $R_2^2(12)$ motif. Besides, the hydroxyl oxygen atom participates, as a hydrogen bond acceptor, in a bifurcated C–H···(O, F) hydrogen bond, involving in addition a benzene carbon and a fluorine atom (see Fig. 3). This intermolecular hydrogen bond builds zig-zag infinite chains, which can be described by a $C(9)R_1^2(7)$ first level graph-set. They are related by inversion centres connected through O–H···O dimers, classified as $R_2^2(12)$, and developing a two-dimensional structure, which extends perpendicular to the *a*-axis (see Fig. 3).

The crystal structure of 3-(hydroxymethyl)chromone, the non-trifluoromethylated analogue of **3**, showed a similar arrangement of dimers generating loops.[72]

3.2. Electrostatic potentials

The molecular electrostatic potential maps (ESP) of **1–3**, **5** and **6** (Fig. S6, ESI†) display electrostatic complementarity in the crystal packing for all structures, and reveal the existence of highly polar molecules. The deepest red regions in each surface

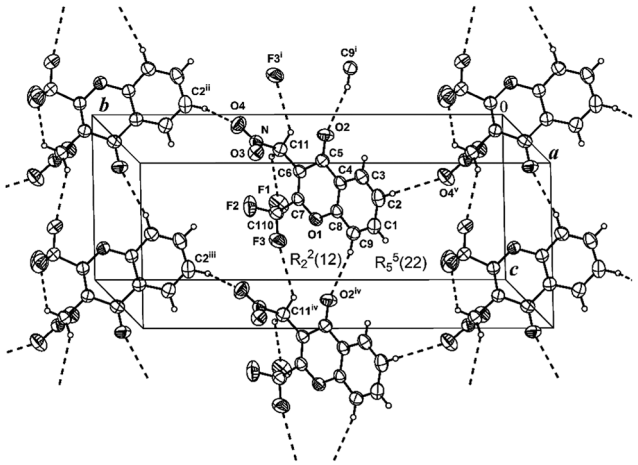

Fig. 2 C–H···O and C–H···F hydrogen bonds (dashed lines) for **2** showing the $R_2^2(12)$ and $R_5^5(22)$ graph-set motifs, the atom labeling and their displacement ellipsoids at the 30% probability level. Symmetries operations: (i) *x*, *y*, −1 + *z*; (ii) 1/2 − *x*, 1/2 + *y*, −*z*; (iii) 1/2 − *x*, 1/2 + *y*, 1 − *z*; (iv) *x*, *y*, 1 + *z*; (v) 1/2 − *x*, −1/2 + *y*, −*z*.

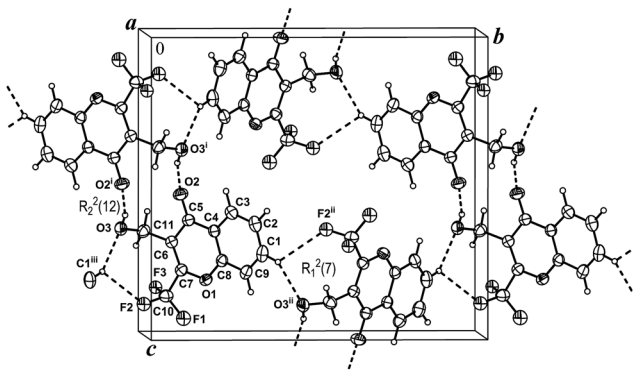

Fig. 3 O–H···O, C–H···O and C–H···F hydrogen bonds (dashed lines) for **3** showing the $R_1^2(7)$ and $R_2^2(12)$ graph-set motifs, the atom labeling and their displacement ellipsoids at the 30% probability level. The figure illustrates the replica of the rotationally disordered $-CF_3$ group with the largest occupancy [0.311(8)]. Symmetries operations: (i) −*x*, −*y*, 1 − *z*; (ii) −1/2 − *x*, 1/2 + *y*, 3/2 − *z*; (iii) −1/2 − *x*, −1/2 + *y*, 3/2 − *z*.

correspond to strongly electronegative potential (average −0.061 a.u.) surrounding the carbonyl O2 oxygen atom and the deep blue region of electropositive potential (average 0.055 a.u.) is near the H9 (H for structure **3**) hydrogen atom. The highly electronegative oxygen atom causes the highest electropositive value (0.138 a.u.) around the H atom in the O–H group of **3**. Interestingly, light red regions can be observed around the fluorine atoms with low electronegative potentials (average −0.011 a.u.) interacting with blue electropositive regions near the phenyl hydrogen atoms of the surface. These results provide clear evidence of relatively strong O–H···O and C–H···O hydrogen bonds as well as weak C–H···F hydrogen bonds in these structures.

3.3. Intermolecular interaction energies

The calculated lattice energies obtained by the PIXEL program for **1–3**, and **5–6** are summarized in Table S14 (ESI†). In Table 2 are listed the intermolecular interaction energies computed at the MP2/6-31G(d,p) level (E_{MP2}), together with those obtained using the PIXEL program (E_{TOT}), which allow a quantitative decomposition of the interaction energies into their various physical terms. The *ab initio* calculations were performed using the counterpoise method considering the basis set superposition error. All calculations were performed, for diverse molecular pairs, at the in-crystal geometry. In Table 2 are also indicated the selected hydrogen bonds and π-stacking interactions, as well as the symmetry operation relating molecular pairs. A careful inspection of the interaction energies reveals that the E_{MP2} values agree well with E_{TOT} obtained by the PIXEL program.

In all molecular pairs, there are C–H···F interactions in competition with C–H···O, C–H···N (only in **1**) and C–H···Br (only in **6**) hydrogen bonds. In addition, the supramolecular networks of the title compounds include the existence of intermolecular π···π interactions with offset facial arrangement,[74–76] involving the pyran (Cg1 centroid) and benzene (Cg2 centroid) rings of the chromone system (Table S15, ESI†). Intermolecular energies corresponding to molecular pairs involving only π···π interactions (Table 2) are notably high for compounds **1** (−42.3 kJ mol^{-1}), **3** (−24.4 kJ mol^{-1}) and **5** (−31.9 kJ mol^{-1}), indicating an important contribution towards the crystal packing in these structures. In **1**, the chains are formed by CH···F contacts with cohesive energy of −4.7 kJ mol^{-1}, and the contribution of CH···O and CH···N bonds with intermolecular energies between −12.3 and −29.8 kJ mol^{-1}. Besides, π···π interactions with the largest contribution to intermolecular energy, between −35.4 and −42.3 kJ mol^{-1} are also involved. PIXEL intermolecular energies decomposition reveal that C–H···F hydrogen bonds and π···π interactions possess a dispersive nature, while C–H···O and C–H···N hydrogen bonds present a higher electrostatic contribution. In addition, NBO calculation for compound **1** also evidences the likely quantum-mechanical nature of C–H···N and C–H···O hydrogen bonds, their contributions to the stabilization energy is the largest at about −6.7 and −8.2 kJ mol^{-1}, respectively. Similar results on the character of these weak intermolecular interactions were found for the other analyzed structures (**2–6**), but with a more significant contribution of charge transfer to the intermolecular π···π interaction, of about −8.5 and −11.5 kJ mol^{-1}. These weak hydrogen bond interactions, such as single C–H···F contacts, cannot be ignored in the building of supramolecular architectures, since the total interaction energy represents the cooperative effect contributing towards the stability of crystal packing.[74] The largest intermolecular energy value observed in Table 2 (−49.9 kJ mol^{-1}) corresponds to the O–H···O hydrogen bond between the hydroxyl group and the carbonyl oxygen atom in **3**. This interaction accounts also with the highest directionality and the shortest intermolecular O···O distance (2.830(3) Å). It supports our previous finding that the strength and importance of this interaction is of such magnitude that it might be one of the causes that prevent the formation of the C–H···O and C–H···F hydrogen bonds, building the $R_2^2(12)$ second level graph set in **1** and **2**. Besides, the NBO analysis predicted a value of −40.7 kJ mol^{-1} for this O–H···O contact. There are two

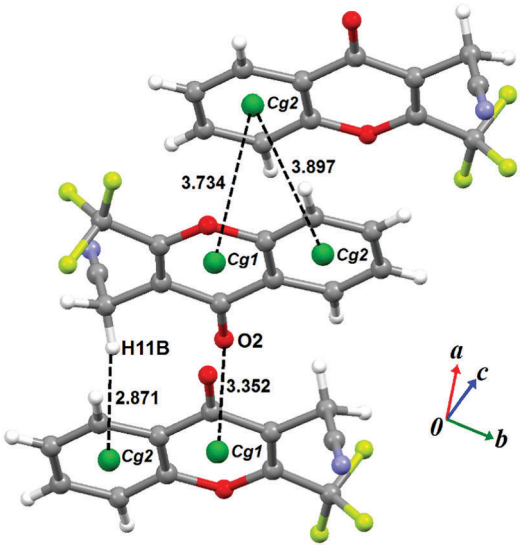

Fig. 4 A view of the π···π stacking, C–H···π and C═O···π (dashed lines) interactions showing intercentroid, H···Cg2 and O···Cg1 distances for compound **1**.

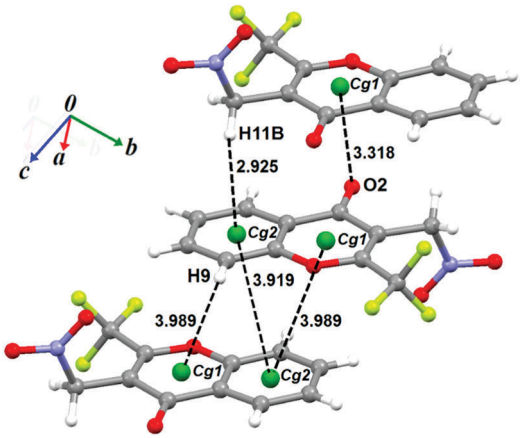

Fig. 5 A view of the π···π stacking, C–H···π and C═O···π (dashed lines) interactions showing intercentroid, H···Cg and O···Cg1 distances for compound **2**.

O–H···O hydrogen bonds in the molecular pair and their contribution to the interaction energy is of the same order of magnitude as the coulombic component, −71.9 kJ mol^{-1} (Table 2), indicating that charge transfer would also contribute significantly to the O–H···O hydrogen bond energy.

The contribution to the crystal stability of the C═O···π interactions, in compounds **1** (Fig. 4), **2** (Fig. 5) and **5**, was also analyzed from structural data obtained by X-ray diffraction (see Table 3) and NBO analysis. Unlike structures **1** and **2**, where the carbonyl group interacts almost parallel to the aromatic plane (∠C5–O2···Cg(1) = 87°), in **5** it points nearly perpendicular to the center of the aromatic plane as reflected by the highest directionality of 159°. This preferential orientation along with the shortest O2···Cg(1) distance of 2.9334(2) Å indicates that C═O···π interaction is stronger for compound **5** (Fig. S7, ESI†), in comparison to those of structures **1** and **2**. The NBO calculations confirm that this interaction has the largest contribution in **5**, but in all cases with values below |−3 kJ mol^{-1}|, resulting in a very small contribution to the stabilization energy.

The C–H···π contacts between methylene hydrogen atoms and benzene rings are other interactions that could contribute to the molecular packing energy in **1** and **2**, as described in Table 3. The –CN and –NO_2 groups possessing linear and trigonal planar geometries, respectively, are arranged in the crystal lattice so that the H11B atoms come close to the neighboring benzene ring, and favor the C–H···π interactions. However, no significant charge transfer was observed between the corresponding interacting natural atomic orbitals for these contacts.

3.4. The main intermolecular contacts according to the Hirshfeld approach

The main intermolecular interactions found in the crystals of **1–3** and the closely related homologous **5** and **6** were quantified using Hirshfeld surface analysis. Fig. 6 shows this type of surface for **1–3** mapped over the d_{norm} property, which is transparent enough to allow the molecules to be viewed in a similar orientation. The deep red circular regions visible on the front and back view (180° rotated around the plot vertical axis) of the surfaces are indicative of hydrogen bonds (Table 2) and other close contacts. For comparison, the d_{norm} surfaces of **5** and **6** were also calculated (Fig. S9, ESI†).

Fig. 7 shows shape index and curvedness surfaces for **1–3** (for the corresponding surfaces of **5** and **6**, see Fig. S10, ESI†). The pattern of alternated red and blue triangles on the shape index surfaces (column 1) shows π···π stacking arrangement of six-membered rings.[33] The red triangles are concave regions associated with atoms of the π···π stacked rings above them, while the blue triangles are convex regions indicating the aromatic ring atoms of the molecule inside the surface. The π···π interactions are also evident as relatively large and green

Table 3 Geometrical parameters of C–Y···π interactions[a] for compounds **1–3** and **5** (Å, °)

Compound	C–X(*i*)···Cg(*j*)[b]	X···Cg	X-Perp[c]	γ[d]	∠C–Y···π X···Cg(*j*)	Symmetry
1	C5–O2···Cg(1)	3.3515(4)	3.332	6.26	87	$-x, -y, -z$
	C11–H11B···Cg(2)	2.87	2.86	4.60	135	$-x, -y, -z$
2	C5–O2···Cg(1)	3.3178(3)	3.289	7.49	87	$1-x, -y, 2-z$
	C11–H11B···Cg(2)	2.92	2.92	3.45	131	$1-x, -y, 2-z$
3	C10–F3A···Cg(1)	3.2321(1)	2.848	28.22	129	$1+x, y, z$
5	C5–O2···Cg(1)	2.9334(2)	2.893	9.58	159	$1-x, \frac{1}{2}+y, \frac{1}{2}-z$

[a] (H···Cg < 3.0 Å, O···Cg and F···Cg < 4.0 Å, γ < 30.0°). [b] Centroid of C1–C4/C8–C9 ring for Cg(1) and O1/C4–C8 ring for Cg(2). [c] Perpendicular distance of X to ring plane J. [d] Angle between the Cg–X vector and ring J normal.

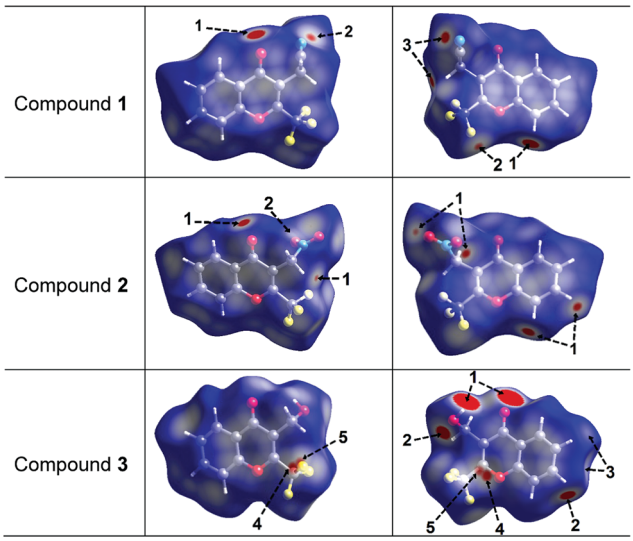

Fig. 6 Views of the Hirshfeld surfaces, mapped over the d_{norm}, in two orientations for compounds **1–3**. The surfaces in the last column are 180° rotated around the vertical axis of the plot. Labels denote hydrogen bonding contacts: 1: C–H···O; 2: C–H···F; 3: C–H···N; 4: C=O···π; 5: F···F.

flat regions delineated by a blue outline in the corresponding *Curvedness* surfaces (column 2).[77] However, these features are not exactly observed in the surfaces rotated by 180° (columns 3 and 4 for compounds **1**, **2** and **5**), which reveal π-stacking with different ways of contact between the adjacent molecules on both sides of the surface. Besides, C–H···π interactions are only observed in structures **1** and **2** as 'bow-tie' patterns of large red and blue triangles on shape index surfaces (column 3). The π···π stacking interactions are recognizable in **3** and **6** on rotated surfaces mapped with shape index and *curvedness* functions (columns 3 and 4).

The fingerprint plots of the main intermolecular contacts for structures **1–3** (Fig. 8) and the related structures **5** and **6** (Fig. S11, ESI†) are shown. The pair of narrow spikes labeled 1 corresponds to the shortest O···H interactions associated with C–H···O hydrogen bonds and those labeled 2 show the presence of F···H indicating C–H···F hydrogen bonds. Moreover, the broad wings referred to as 3 are characteristic of C···H contacts associated with C–H···C hydrogen bonds including C–H···π interactions. The region of pale blue to green colour (labeled 8) on the diagonal at around $(d_e + d_i)$ = 1.8 Å in structures **1–3**, **5** and **6** depicts C···C contacts characteristic of π-stacking interactions,[33] which confirm the results of *shape index* and *curvedness* surfaces above-mentioned. The relative contributions of the intermolecular contacts to the Hirshfeld surface area for **1–3**, **5** and **6** are shown as a histogram in Fig. 9. The F···H contacts have the major contribution (21–40%) due to the relatively high proportion of terminal fluorine atoms in the molecules. The C···H contacts are in the 11–15% range for compounds **1–3**, and **5** but falls to 8% in **6**. This result reveals that C···C and C···H contacts are presumably in competition.[78] A noticeable F···F contact ranging from 2 to 9% in all structures is indicative of relatively strong dipole–dipole interactions that provide stability to the crystal structures.[28]

3.5. Enrichment ratios

The enrichment ratio[78] is a new indicator derived from Hirshfeld surface analysis, in order to examine the propensity of two chemical species (X, Y) to be in contact. The enrichment ratio E_{XY} is defined as the ratio between the proportion of actual contacts C_{XY} in the crystal, and the theoretical proportion of random contacts R_{XY}. The proportion S_X of different chemical species on the molecular surface is obtained from C_{XX} and C_{XY} values. The random contacts R_{XY} values are calculated from the corresponding S_X and S_Y proportions using probability products.

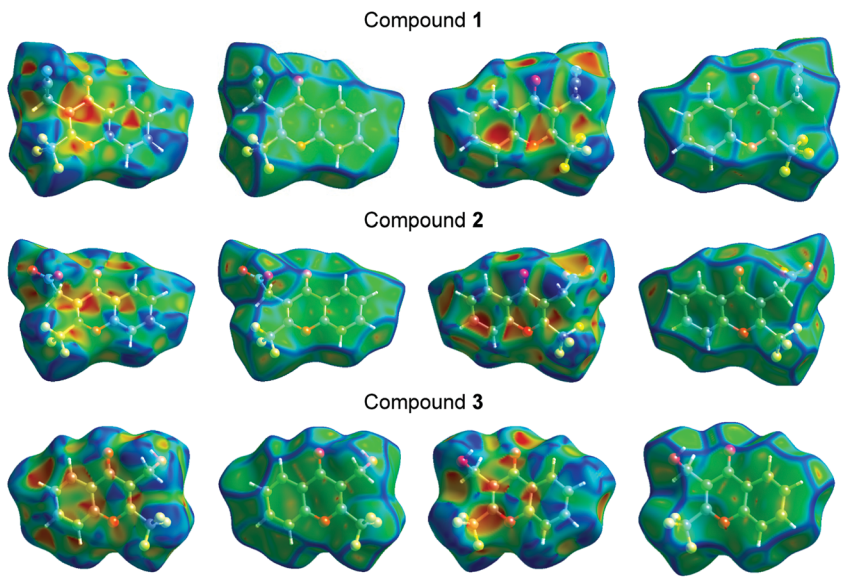

Fig. 7 Hirshfeld surfaces mapped with shape index and *curvedness* for compounds **1–3**. The surfaces in columns 3 and 4 are 180° rotated around the vertical axis of the plot.

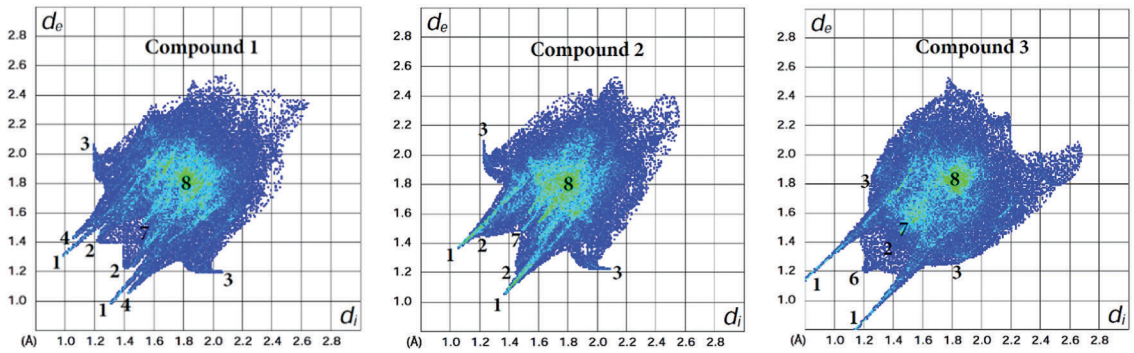

Fig. 8 Fingerprint plots of compounds **1–3**. Close contacts are labelled as: (1) O···H, (2) F···H, (3) C···H, (4) N···H, (6) H···H, (7) F···F and (8) C···C.

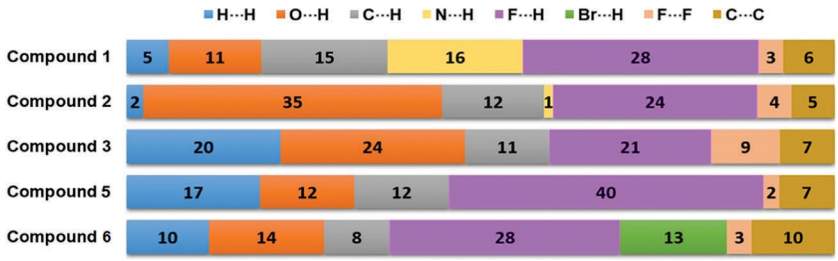

Fig. 9 Relative (%) contributions of the main intermolecular contacts to the Hirshfeld surface area for compounds **1–3** and **5**, **6**.

The value of E_{XY} is expected to be generally larger than unity for pairs of elements with high propensity to form contacts in crystals, while pairs that tend to avoid them are associated with E_{XY} values lower than unity.

Table 4 shows the enrichment ratios of the main intermolecular contacts for compounds **1–3**, **5** and **6** (complete information is provided in Tables S16 and S17, ESI†). The E_{FH} ratios larger than unity (1.03–1.78) in all compounds indicate that C–H···F hydrogen bonds have a high tendency to form in crystals,[79] comparable to stronger O···H contacts (E_{OH} = 1.09–2.05) associated with C–H···O and O–H···O hydrogen bonds. In comparison to the remaining structures, the values of 1.78 for compound **5** and 2.05 for compound **2** can be attributed to the highest proportion of fluorine (25.0%) and oxygen (23.4%), respectively, at the corresponding molecular surfaces. The C···H contacts appear enriched only for compounds **1** (E_{CH} = 1.03) and **2** (E_{CH} = 1.13), and they are involved in C–H···π interactions as described in Table 2.

Table 4 Enrichment ratios E_{XY} of the main intermolecular contacts for compounds **1–3**, **5** and **6**

Interaction	1	2	3	5	6
C···H	1.03	1.13	0.74	0.73	0.60
N···H	1.93	[a]	—	—	—
O···H	1.43	2.05	1.75	1.09	1.66
F···H	1.62	1.48	1.03	1.78	1.56
Br···H	—	—	—	—	1.40
C···C	1.98	2.58	2.89	2.41	4.07
C···O	1.38	0.85	0.23	1.85	1.00

[a] E_{XY} values for random contacts R_{XY} lower than 0.7% were not calculated.

Moreover, C···C contacts represent π-stacking interactions, which are remarkably enriched in all five structures (E_{CC} = 1.98–4.07) as expected for molecules with low hydrogen content.[79]

The occurrence of C═O···π contacts for structures **1**, **2** and **5**, with higher intermolecular energies of −35.4, −37.5 and −20.9 kJ mol^{-1}, respectively, was also predicted by calculation of enrichment ratios. E_{CO} values higher than unity for compounds **1** (1.38) and **5** (1.85), and slightly smaller than unity for compound **2** (0.85) indicate that the O···π contact is a favorable interaction which contributes to the stability of crystal structures. Other weak interactions are present together with the C═O···π contacts revealing the influence of cooperative effects in the high intermolecular energy values observed for these compounds (Table 2).

3.6. The expected conformation of the "free" molecule

All compounds (**1–4**) possess C_1 symmetry. The conformational study for all structures was carried out with the B3LYP/6-311++g(d,p) level of theory. The conformational rearrangement of the substituent with respect to the molecular plane was evaluated from the potential relative curves. They were obtained by internal rotation around the C5C6–CH_2R bond. The dihedral angle calculated at the most stable conformation for each compound is (see Fig. S12a–d, ESI†): **1**: C5C6–C11C12, −101.3°; **2**: C5C6–C11N, −98.5°; **3**: C5C6–C11O3, 57.3° and **4**: C5C6–C11N, 66.0°. Considering the experimental values obtained by X-ray diffraction, it can be noted that compound **1** and **2** exhibit the –CN and –NO_2 groups arranged on the same side of the molecular plane (observed: −75.4° and −82.6°, for **1** and **2**, respectively), whereas the hydroxyl group is predicted on the

Table 5 Selected experimental and calculated frequencies (cm^{-1}) and tentative fundamental vibration modes assignment of **1–4**[a]

	1 (–CN)				**2** ($–NO_2$)				**3** (–OH)				**4** ($–NH_2$)			
	Exp.		Calc.[c]		Exp.		Calc.		Exp.		Calc.		Exp.		Calc.	
Assignment[b]	IR	Raman	Freq.	Int.	IR[a]	Raman	Freq.	Int.	IR	Raman	Freq.	Int.	IR	Raman	Freq.	Int.
ν(O–H)									3438(m)	3437(6)	3758	71				
$\nu_{as}(NH_2)$													3328(w)	3329(16)	3606	7
$\nu_{s}(NH_2)$														3222(16)	3522	<1
$\nu_{as}(CH_2)$	3025(vw)	2997(23)	3116	3		3026(5)	3177	2	2948(vw)	2951(2)	3147	9	2920(w)	2877(19)	3100	2
$\nu_{s}(CH_2)$	2997(w)	2938(32)	3063	10	3032(w)	2970(8)	3107	10	2902(vw)	2903(2)	3002	31	2845(w)	2841(18)	3022	44
ν(C–N)	2265(w)	2264(25)	2357	13												
ν(C5–O2)	1654(m)	1652(100)	1709	295	1659(vs)	1654(100)	1713	308	1646(vs)	1651(100)	1688	330	1659(m)	1661(80)	1714	302
ν(C6–C7)	1612(w)	1612(27)	1674	88	1613(m)	1643[sh](8)	1675	103	1610(m)	1638[sh](10)	1666	47	1612(w)	1652(100)	1671	50
$\delta(NH_2)$													1581(w)	1641(56)	1655	46
$\nu_{as}(NO_2)$					1567(vs)		1632	358								
$\nu_{s}(NO_2)$					1422(m)		1418	159								
$\nu_{as}(CF_3)$	1159(vs)	1157(9)	1136	283	1160(vs)	1174(2)	1136	269	1151(vs)	1153(5)	1128	211	1168(m)		1172	123
ν(C11–N)					865(w)	895(12)	899	17					1115(m)	1041(17)	1057	19
ν(C11–O3)									1036(m)	1036[sh](5)	1060	108				
γ(C11–O3–H)									591(w)	594(5)	571	170				

[a] vs, very strong; s, strong; m, medium; w, weak; vw, very weak; sh, shoulder. [b] ν, δ, and γ represent stretching, in-plane deformation, out-of-plane deformation. [c] 6-311++g(d,p) calculated IR frequencies (cm^{-1}) and intensities (km mol^{-1}).

opposite side compared with that found in the solid (−77.8° for **3**, see Table S1, ESI†). As described above, the molecules of **3** are disposed as centrosymmetric dimers through strong OH···O=C bonds. This difference is because calculations are performed for isolated molecules, and therefore they do not consider the intermolecular contacts acting in the crystal packing, which are responsible for the arrangement found in **3**. Moreover, the $–CF_3$ group shows two different conformations. In **1** and **2** one fluorine atom is oriented *syn* with respect to the C6–C7 double bond (C6C7–C10F = −1.8° and −7.4°, respectively), and *anti* in **3** and **4** (C6C7–C10F = −179.7° and −167.8°, respectively).

3.7. Molecular interaction in the solid state revealed by vibrational spectroscopy

A complete tentative assignment of the observed IR and Raman spectra (Fig. S13a–d, ESI†) was performed for **1–4**. Some fundamental vibrational modes possibly the most influenced by the change of substituent at the CH_2 group are shown in Table 5 (full assignment in Tables S18–S21, ESI†). A detailed vibrational description for the chromone skeleton was published elsewhere.[43,80] The asymmetric and symmetric stretching of the $–CH_2–R$ (R = CN, NO_2, OH, NH_2) moiety appeared as very weak IR absorption bands at 3025, 3052, 2948 and 2920 cm^{-1} (Raman: 2997, 3026, 2951 and 2877 cm^{-1}) and 2997, 3032, 2902 and 2845 cm^{-1} (Raman: 2938, 2970, 2903 and 2841 cm^{-1}), for **1–4**, respectively. Therefore, for both $–CH_2$ stretching modes, the electron withdrawing effect of the substituents on the observed absorption frequencies exhibited the following trend: $NO_2 > CN > OH > NH_2$.

The IR spectrum of **1** (Fig. S13a, ESI†) shows the characteristic stretching band of the cyano group at 2265 cm^{-1} (Raman: 2264 cm^{-1}). For **2** and **4** (NO_2 and NH_2) the IR absorptions attributed to the C–N stretching are located at 865 and 1115 cm^{-1} (Raman: 895 and 1041 cm^{-1}) as weak and medium intense bands, respectively (Fig. S13b and d, ESI†). For both compounds, the observed frequencies (IR and Raman) are in agreement with similar modes in related molecules.[81,82] For **3** a characteristic IR band at 3438 cm^{-1} (Raman: 3437 cm^{-1}) is assigned to the OH stretching vibration. The strong broad band and its location suggest the existence of intermolecular hydrogen bonding. The stretching of the carbonyl (C=O) groups is attributed to the very strong IR bands at 1654, 1659, 1646 and 1659 cm^{-1} (Raman: 1652, 1654, 1651 and 1661 cm^{-1}) for **1–4**, respectively. In compounds **2** and **4** ($–NO_2$ and $–NH_2$, respectively) the C=O band is slightly shifted to higher wavenumbers in comparison with **1** and **3** (–CN and –OH, respectively). This fact can be explained considering the different strength and nature of the hydrogen bonds (see Fig. 1–3), that can be visualized through the O···H distances (**1**: 2.401 Å; **2**: 2.563 Å; **3**: 1.925 Å) obtained by X-ray diffraction. For compounds **1–4**, the C6–C7 double bond stretching bands of the heterocycle are assigned to the IR bands at 1612, 1613, 1610 and 1612 cm^{-1}, respectively, showing no significant differences between them.

3.8. Molecular behavior in solution determined by UV-Vis and NMR spectroscopy

The electronic absorption spectra of **1–4** were recorded in the spectral range of 200–1100 nm using methanol as a solvent (5.57×10^{-5} M (**1**), 4.57×10^{-5} M (**2**), 6.76×10^{-6} M (**3**) and 5.9×10^{-5} M for (**4**)) and are shown in Fig. S14 (ESI†). In Table 6 the main absorption bands are described and correlated with the calculated values. Also a tentative assignment of the electronic transitions supported by theoretical calculations and related compounds[43,80] is presented for **1–4**. Only the dominant transitions were considered to assign the observed bands.

All compounds (**1–4**) show maximum absorption bands at around 205 nm. Moreover, the electronic transitions with dominant oscillator strength (0.365, 0.307, 0.311 and 0.225) are attributed to HOMO−1 → LUMO+1, HOMO−3 → LUMO+2, HOMO−2 → LUMO+1 and HOMO−2 → LUMO+2 excitations for **1–4**, respectively. The well-defined broad bands, observed in the electronic spectra of **1–4**, with absorptions at 300, 302,

Table 6 Observed electronic spectra of **1–4** in methanol solution along with calculated electronic transitions relevant for the assignments

1 (CN)			**2** (NO_2)			**3** (OH)			**4** (NH_2)		
Exp.[a]	Calc.[b]	Assignment	Exp.	Calc.	Assignment	Exp.	Calc.	Assignment	Exp.	Calc.	Assignment
204	202(0.133)	H−2 → L + 2 (74%)	204	198(0.131)	H → L + 3 (49%)	204	203(0.311)	H−2 → L + 1 (29%)	205	203(0.225)	H−2 → L + 2 (43%)
	203(0.365)	H → L + 2 (32%)			H−3 → L + 2 (16%)			H−1 → L + 2 (26%)			H−3 → L + 1 (23%)
		H−1 → L + 1 (22%)			H−1 → L + 3 (13%)			H → L + 2 (24%)			H−1 → L + 2 (18%)
		H−2 → L + 2 (23%)		205(0.307)	H−3 → L + 2 (31%)		205(0.093)	H−1 → L + 2 (68%)		205(0.211)	H−2 → L + 2 (45%)
221	229(0.206)	H−3 → L (75%)			H−1 → L + 2 (21%)			H → L + 2 (13%)			H−3 → L + 1 (22%)
		H → L + 2 (11%)			H−1 → L + 3 (14%)	222	232(0.282)	H−4 → L (64%)			H−1 → L + 2 (14%)
245	244(0.196)	H → L + 1 (76%)			H → L + 3 (21%)			H → L + 1 (19%)	225	231(0.152)	H−4 → L (42%)
251[sh c]	270(0.106)	H−1 → L (84%)	220[sh c]	220(0.088)	H−1 → L + 2 (44%)	243	243(0.197)	H → L + 1 (61%)			H−2 → L + 1 (36%)
300	301(0.094)	H → L (91%)			H−4 → L (27%)			H−4 → L (19%)			H−1 → L + 1 (11%)
					H−3 → L + 2 (10%)			H−2 → L (11%)		233(0.084)	H−2 → L + 1 (60%)
			246	234(0.118)	H−3 → L (65%)	250[sh c]	268(0.102)	H−2 → L (80%)			H−4 → L (31%)
					H−5 → L + 1 (11%)			H → L + 1 (11%)	244	242(0.209)	H → L + 1 (61%)
			255[sh c]	272(0.060)	H−1 → L (64%)	303	299(0.095)	H → L (91%)			H−4 → L (14%)
					H−2 → L + 1 (13%)						H−3 → L (13%)
			302	301(0.096)	H → L (84%)				253[sh c]	265(0.077)	H−3 → L (81%)
											H−1 → L + 1 (10%)
									305	295(0.097)	H → L (84%)

[a] Absorption maxima spectral positions are given in nm. [b] Oscillator strengths of calculated transitions, shown in parenthesis, are in atomic units. [c] Shoulder.

303 and 305 nm, respectively, are attributed to HOMO → LUMO excitations. For compounds **1–3** they are originated by π → π* transitions from π-bonding orbitals of the aromatic ring to π-antibonding orbitals of the heterocyclic ring. While for **4**, this electronic transition includes excitations from $n_{(NH_2)}$ to π* orbitals of both fused rings. The main molecular orbitals involved in the electronic transitions of all compounds are depicted in Fig. S15–S18 (ESI†).

The ^{1}H and ^{13}C NMR chemical shifts (δ) for **1–4** are shown in Table 7. Calculated data were performed with the GIAO method,[58] after full geometry optimization with the GAUSSIAN 09 program.[57] Comparing the experimental and theoretical data for protons, a good agreement is observed with $\Delta = \delta_{exp} - \delta_{calc}$ deviation ranging from −0.43 to −0.09 ppm. Due to the strong dependence of the experimental conditions, the acidic protons of the amino group were not considered in the correlations. The linear relationship between calculated and experimental data ($\delta_{calc} = b\delta_{exp} + a$) for ^{1}H and ^{13}C gives the following correlations: **1**, ^{1}H: $R^2 = 0.996$, $a = -0.092$, $b = 1.04$, ^{13}C: $R^2 = 0.995$, $a = 1.462$, $b = 1.034$; **2**, ^{1}H: $R^2 = 0.999$, $a = -0.191$, $b = 1.05$, ^{13}C: $R^2 = 0.992$, $a = 5.14$, $b = 1.0$; **3**, ^{1}H: $R^2 = 0.999$, $a = -0.11$, $b = 1.07$, ^{13}C: $R^2 = 0.995$, $a = 6.82$, $b = 1.0$; **4**, ^{1}H: $R^2 = 0.998$, $a = -0.1291$, $b = 1.051$, ^{13}C: $R^2 = 0.990$, $a = 1.18$, $b = 1.04$ (Fig. S19a–h, ESI†).

The experimental and theoretical data of ^{13}C NMR correlate very well except for carbon atoms in position 3. The greatest discrepancy was found for **4** ($\Delta = -12.8$ ppm, see Table 7). Similar results were found for carbon atoms directly attached to the electron-withdrawing trifluoromethyl group[43,81] and were also reported by other authors in related halogenated compounds.[83] The proton chemical shift of the methylene moiety is strongly influenced by the directly bonded substituent group. Compared with **5** (R = H), the observed deshielding follows the standard electronegativity trend of the substituents: (ppm) NO_2 (5.64) > OH (4.76) > NH_2 (3.93) > CN (3.80) > H (2.23).[43] A similar behavior was found in ^{13}C NMR for the methylene carbon atom. (ppm) NO_2 (66.7) > OH (55.5) > NH_2 (42.2) > CN (12.2) > H (8.7).[43] Here, the lower influence of the CN group could be attributed to the anisotropic diamagnetic shielding of the CN triple bond. The broad signals of the acidic protons of the amine and hydroxyl groups are localized at 3.26 and 3.18 ppm for **3** and **4**, respectively.

3.9. Molecular docking

Docked solutions with the lowest binding energy were selected and described. The binding free energy of compounds **1** (–CN), **2** (–NO_2), **3** (–OH) and **4** (–NH_2) were −7.1, −7.1, −7.6 and −7.8 kcal mol^{-1}, respectively. The higher binding energy calculated for **4** and **3** is mainly due to the number of H-bonds detected (three and two H-bonds for **4** and **3**, respectively) compared with only one H-bond for **1** and **2**. As shown in Table 8, several enzyme–ligand van der Waals interactions were detected for **1–4**. The sum of all van der Waals contacts may form

Table 7 Comparison between experimental and calculated NMR chemical shifts (in ppm) of **1–4**[a]

	1 (CN)			**2** (NO_2)			**3** (OH)			**4** (NH_2)		
	Exp.	Calc.[b]		Exp.	Calc.		Exp.	Calc.		Exp.	6-311+g(2d,p)	
CH_2	3.8	3.9	(−0.1)	5.64	5.80	(−0.16)	4.76	4.87	(−0.11)	3.93	4.02	(−0.09)
OH	—	—	—	—	—	—	3.18	3.34	(−0.16)	—	—	—
NH_2	—	—	—	—	—	—	—	—	—	3.26	1.27	(1.99)
H-5	8.2	8.65	(−0.45)	8.23	8.65	(−0.42)	8.19	8.64	(−0.45)	8.19	8.62	(−0.43)
H-6	7.52	7.66	(−0.14)	7.55	7.68	(−0.13)	7.48	7.87	(−0.39)	7.45	7.62	(−0.17)
H-7	7.81	7.99	(−0.18)	7.84	8.00	(−0.16)	7.77	8.16	(−0.39)	7.74	7.86	(−0.12)
H-8	7.56	7.72	(−0.16)	7.6	7.76	(−0.16)	7.53	7.91	(−0.38)	7.5	7.71	(−0.21)
C-2	150.5	158.2	(−7.7)	152.9	161.2	(−8.3)	149.5	157.0	(−7.5)	149.9	156.6	(−6.7)
C-3	114.8	124.2	(−9.4)	113.7	119.9	(−6.2)	122.7	131.7	(−9)	121.6	134.4	(−12.8)
C-4	175.4	179.2	(−3.8)	175.7	179.9	(−4.2)	179	185.4	(−6.4)	177.9	182.8	(−4.9)
C-5	127.1	133	(−5.9)	127.3	133.1	(−5.8)	126.6	131.1	(−4.5)	126.4	132	(−5.6)
C-6	126.3	130.9	(−4.6)	126.5	131.4	(−4.9)	126	131.6	(−5.6)	126.2	130.2	(−4)
C-7	135.7	139.5	(−3.8)	135.9	139.7	(−3.8)	135.4	140.7	(−5.3)	135.1	138.5	(−3.4)
C-8	118.4	121.8	(−3.4)	118.6	122.3	(3.7)	118.5	123.1	(−4.6)	118.3	122.2	(−3.9)
C-4a	122.2	128.4	(−6.2)	122.6	128.9	(−6.3)	123	128.9	(−5.9)	122.9	129.4	(−6.5)
C-8a	155	161.9	(−6.9)	155.2	161.2	(−6.0)	155.2	162.0	(−6.8)	155.1	161.7	(−6.6)
$\underline{C}H_2R$	12.2	12.1	(0.1)	66.7	70.6	(−3.9)	55.5	61.8	(−6.3)	42.2	41.8	(0.4)
CN	115.6	119.2	(−3.6)	—	—	—	—	—	—	—	—	—
CF_3	119.1	131.2	(−12.1)	119.1	131.2	(−12.1)	119.5	131.5	(−12.0)	119.6	131.9	(−12.3)

[a] $\Delta = \delta_{exp} - \delta_{calc}$ values in parentheses. The standard numbering scheme of the benzopyrane skeleton was adopted for atom labeling (see Scheme 1). [b] B3LYP/6-311+g(2d,p) calculated chemical shifts.

a cluster of weak interactions that stabilize the connection of each molecule with the substrate binding site of the enzyme.

Some differences were found in the way that the investigated molecules interact with PLA2. The planar chromone molecular skeleton showed the same orientation in the binding pocket of PLA2 for all compounds, even though the substituent in C6 presents different orientations. Compounds **1** and **2** could form H-bonds between O2 and His48 in the active site of the enzyme and the docking results suggested van der Waals interactions between the nitrile moiety and Leu2 and Tyr52 that favor that orientation (Fig. S25a and b, ESI†). For compounds **3** and **4**, the C6 substituent took the opposite orientation due to the H-bond interactions; compound **3** formed H-bonds with Cys45 and Asp49, and compound **4** with Cys29, Cys45 and Asp49. Such interactions are meaningful to evaluate, since they hinder the normal catalysis cycle of the enzyme. The catalytic mechanism of PLA_2 implies water activation by His48 for the subsequent nucleophilic attack of sn2 ligation of the glycerophospholipids that will be hydrolyzed.[21] Similar results were found for a biflavonoid.[84] Moreover, the amino group is an interesting substituent and as is shown in Fig. 10a, the nitrogen atom of compound **4** could act as a proton acceptor forming three N–H bonds with the side chain acidic protons of Cys29, Cys45 and Asp49. The oxygen atom is also able to act as a proton acceptor. The hydroxyl substituent of compound **3** shows two O–H bonds with Cys45 and Asp49 (see Fig. 10b). Apparently, the sp^3 –OH is more effective than the sp^2 carbonyl oxygen atom to form H-bonds. However, compounds **1** and **2** form one H-bond through the carbonyl group (see Fig. S25a and b, ESI†). A series of thiobenzoic acid *S*-benzyl esters showed analogous results.[85] Such interactions could also displace the Ca^{2+}-coordinated ion, which is required for the catalysis.[21] As shown in Table 8, several enzyme–ligand van der Waals interactions were detected for **1–4**. The sum of all van der Waals contacts may form a cluster of

Table 8 Docking results between compounds and *Crotalus durissus terrificus* PLA2

	1 (CN)			**2** (NO_2)			**3** (OH)			**4** (NH_2)		
Residue	vdW[a]	H-Bond[b]	π···π[c]	vdW	H-Bond	π···π	vdW	H-Bond	π···π	vdW	H-Bond	π···π
Leu2	✓			✓			✓			✓		
Phe5			✓			✓			✓			✓
Asn6	✓			✓			✓			✓		
Ile9	✓			✓			✓			✓		
Tyr22	✓			✓			✓			✓		
Cys29	✓			✓			✓				✓	
Trp31	✓			✓			✓			✓		
Cys45	✓			✓				✓		✓	✓	
His48		✓			✓		✓					
Asp49	✓			✓				✓		✓	✓	
Tyr52	✓			✓			✓			✓		
Leu106	✓			✓			✓			✓		

[a] van der Waals interaction. All residues within 3.5 Å were considered. [b] Hydrogen bond. [c] π···π interaction.

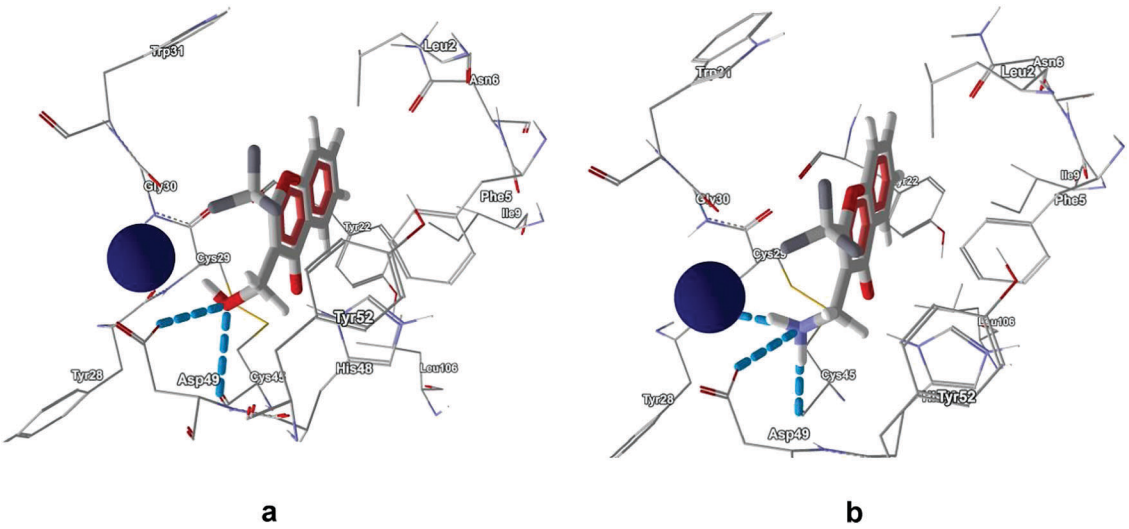

Fig. 10 Docking results between compounds and a snake venom PLA_2 for **3** (a) and **4** (b). Blue spheres represent Ca^{2+} and dotted blue lines hydrogen bonds.

weak interactions that stabilize the connection of each molecule with the substrate binding site of the enzyme. The difference in the higher binding energy calculated for **4** and **3** compared to **1** and **2** is mainly due to the number of H-bonds detected.

Weak interactions play an important role in drug discovery, since most of them interact with their target through H-bonds, π···π stacking and van der Waals interactions, which could be observed between compounds **1–4** and the enzyme.

4. Conclusions

A detailed description of intermolecular hydrogen bonds and π–aromatic interactions in the crystal structures of three novel 2-trifluoromethylchromone derivatives with –CN (**1**), $-NO_2$ (**2**) and –OH (**3**) substituents and two related structures (**5** and **6**) allowed the role that they play in generating different packing motifs controlling the assembly of molecules in the crystal lattice to be understood. Intermolecular interactions were visualized and quantified using Hirshfeld surfaces with two dimensional fingerprint plots. Slight differences in the orientations of the substituents on the 3-methyl group were observed, with the trifluoromethyl group being mainly responsible for the molecular shapes in all the structures. PIXEL, MP2 and NBO interaction energy calculations revealed significant stabilization due to interactions such as hydrogen bonds, π···π stacking, C–H···π and C–O···π contacts, towards the crystal packing in all structures, with important electrostatic contribution. The relative magnitudes of the molecular ESP mapped on Hirshfeld surfaces showed clear evidence about electrostatic effects on the attractive nature of C–H···F hydrogen bonds and other H-bond interactions. Enrichment ratios of H···F contacts in the range of 1.3–1.7 for all compounds indicated that the C–H···F is a favourable interaction, which contributes to the stability of the crystal structures. Intermolecular H-bond, π···π and van der Waals interactions suggested that compounds **1–4** are potential inhibitors of snake venom PLA_2s as is suggested from molecular docking results, and this is an important step to perform *in vitro* and *in vivo* studies. The amino group showed the best binding activity, nevertheless additional studies are required to prove the effectiveness of their biological effects. The vibrational stretching modes and chemical shifts of the methylene group are valuable data to evaluate the effect of the substituent at C-3, both in the solid state and in solution, respectively.

This work represents a substantial effort towards the understanding of intermolecular interactions in chromone systems, particularly providing support and new criteria on the existence of controversial C–H···F hydrogen bonds involving organic fluorine. These results may be important for the design of compounds with novel and improved physical–chemical properties as functional materials, which requires knowledge of supramolecular packing motifs and their experimental control in crystalline lattices.

Conflicts of interest

There are no conflicts to declare.

Acknowledgements

The authors thank Universidad Nacional de La Plata (UNLP), DAAD-Germany, and Departamento de Ciencias Básicas de la Universidad Nacional de Luján for financial support. S. E. U. and J. L. J. specially thank Deutscher Akademischer Austauschdienst Germany (DAAD) for an equipment grant and CONICET (PIP 0359) for financial support. CDAL thanks SENESCYT and CONICET for the fellowship and financial support. The crystallographic work was supported by CONICET (PIP 1529), and by ANPCyT (PME06 2804 and PICT06 2315) of Argentina. S. E. U., G. A. E. and O. E. P. are research fellows of CONICET. J. L. J. is a research fellow of Comisión de Investigaciones Científicas (CIC).

References

1 G. Ellis, *Chemistry of Heterocyclic Compounds: Chromenes, Chromanones, and Chromones*, 1997, vol. 31, pp. 455–480.
2 A. Gaspar, M. J. Matos, J. Garrido, E. Uriarte and F. Borges, *Chem. Rev.*, 2014, **114**, 4960–4992.
3 M. Grazul and E. Budzisz, *Coord. Chem. Rev.*, 2009, **253**, 2588–2598.
4 K. M. Khan, N. Ambreen, U. R. Mughal, S. Jalil, S. Perveen and M. I. Choudhary, *Eur. J. Med. Chem.*, 2010, **45**, 4058–4064.
5 O. Prakash, R. Kumar and V. Parkash, *Eur. J. Med. Chem.*, 2008, **43**, 435–440.
6 M. Isaka, M. Sappan, P. Auncharoen and P. Srikitikulchai, *Phytochem. Lett.*, 2010, **3**, 152–155.
7 J. Rocha-Pereira, R. Cunha, D. C. G. A. Pinto, A. M. S. Silva and M. S. J. Nascimento, *Bioorg. Med. Chem.*, 2010, **18**, 4195–4201.
8 J. H. Park, S. U. Lee, S. H. Kim, S. Y. Shin, J. Y. Lee, C.-G. Shin, K. H. Yoo and Y. S. Lee, *Arch. Pharmacal Res.*, 2008, **31**, 1–5.
9 I. Yousuf, F. Arjmand, S. Tabassum, L. Toupet, R. A. Khan and M. A. Siddiqui, *Dalton Trans.*, 2015, **44**, 10330–10342.
10 C. Zwergel, S. Valente, A. Salvato, Z. Xu, O. Talhi, A. Mai, A. Silva, L. Altucci and G. Kirsch, *MedChemComm*, 2013, **4**, 1571–1579.
11 V. Barve, F. Ahmed, S. Adsule, S. Banerjee, S. Kulkarni, P. Katiyar, C. E. Anson, A. K. Powell, S. Padhye and F. H. Sarkar, *J. Med. Chem.*, 2006, **49**, 3800–3808.
12 K. L. Kirk, *J. Fluorine Chem.*, 2006, **127**, 1013–1029.
13 R. Wilcken, M. O. Zimmermann, A. Lange, A. C. Joerger and F. M. Boeckler, *J. Med. Chem.*, 2013, **56**, 1363–1388.
14 K. L. Kirk, *Org. Process Res. Dev.*, 2008, **12**, 305–321.
15 G. A. Patani and E. J. LaVoie, *Chem. Rev.*, 1996, **96**, 3147–3176.
16 X.-Y. Meng, H.-X. Zhang, M. Mezei and M. Cui, *Curr. Comput.-Aided Drug Des.*, 2011, **7**, 146–157.
17 D.-L. Ma, D. S.-H. Chan and C.-H. Leung, *Chem. Sci.*, 2011, **2**, 1656–1665.
18 F. S. Markland, Jr., *Drugs*, 1997, **54**(suppl 3), 1–10.
19 D. A. Six and E. A. Dennis, *Biochim. Biophys. Acta, Mol. Cell Biol. Lipids*, 2000, **1488**, 1–19.
20 R. Manjunatha Kini, *Toxicon*, 2003, **42**, 827–840.
21 O. G. Berg, M. H. Gelb, M.-D. Tsai and M. K. Jain, *Chem. Rev.*, 2001, **101**, 2613–2654.
22 P. Politzer, J. S. Murray and T. Clark, *Phys. Chem. Chem. Phys.*, 2010, **12**, 7748–7757.
23 G. R. Desiraju, *J. Am. Chem. Soc.*, 2013, **135**, 9952–9967.
24 P. T. A. Galek, J. A. Chisholm, E. Pidcock and P. A. Wood, *Acta Crystallogr., Sect. B: Struct. Sci., Cryst. Eng. Mater.*, 2014, **70**, 91–105.
25 S. M. Soliman, Z. B. Elzawy, M. A. M. Abu-Youssef, J. Albering, K. Gatterer, L. Ohrstrom and S. F. A. Kettle, *Acta Crystallogr., Sect. B: Struct. Sci., Cryst. Eng. Mater.*, 2014, **70**, 115–125.
26 D. J. Wolstenholme, E. J. Fradsham and G. S. McGrady, *CrystEngComm*, 2015, **17**, 7623–7627.
27 P. Panini and D. Chopra, *Cryst. Growth Des.*, 2014, **14**, 3155–3168.
28 H. Sun, U. K. Tottempudi, J. D. Mottishaw, P. N. Basa, A. Putta and A. G. Sykes, *Cryst. Growth Des.*, 2012, **12**, 5655–5662.
29 P. Manna, S. K. Seth, M. Mitra, A. Das, N. J. Singh, S. R. Choudhury, T. Kar and S. Mukhopadhyay, *CrystEngComm*, 2013, **15**, 7879–7886.
30 M. Nishio, *CrystEngComm*, 2004, **6**, 130–158.
31 A. Gambaro, P. Ganis, F. Manoli, A. Polimeno, S. Santi and A. Venzo, *J. Organomet. Chem.*, 1999, **583**, 126–130.
32 S. K. Seth, D. Sarkar, A. D. Jana and T. Kar, *Cryst. Growth Des.*, 2011, **11**, 4837–4849.
33 J. J. McKinnon, M. A. Spackman and A. S. Mitchell, *Acta Crystallogr., Sect. B: Struct. Sci.-Struct. Sci.*, 2004, **60**, 627–668.
34 A. Ruiz, H. Perez, C. Morera-Boado, L. Almagro, C. C. P. da Silva, J. Ellena, J. M. Garcia de la Vega, R. Martinez-Alvarez, M. Suarez and N. Martin, *CrystEngComm*, 2014, **16**, 7802–7814.
35 A. Gavezzotti, *New J. Chem.*, 2016, **40**, 6848–6853.
36 J. D. Dunitz and R. Taylor, *Chem. – Eur. J.*, 1997, **3**, 89–98.
37 D. Chopra and T. N. G. Row, *CrystEngComm*, 2011, **13**, 2175–2186.
38 M. D. Prasanna and T. N. Guru Row, *CrystEngComm*, 2000, **2**, 134–140.
39 E. D'Oria and J. J. Novoa, *CrystEngComm*, 2008, **10**, 423–436.
40 J. D. Dunitz and A. Gavezzotti, *Angew. Chem., Int. Ed.*, 2005, **44**, 1766–1787.
41 V. R. Thalladi, H.-C. Weiss, D. Bläser, R. Boese, A. Nangia and G. R. Desiraju, *J. Am. Chem. Soc.*, 1998, **120**, 8702–8710.
42 L. Shimoni and J. P. Glusker, *Struct. Chem.*, 1994, **5**, 383–397.
43 C. D. Alcívar León, G. A. Echeverría, O. E. Piro, S. E. Ulic and J. L. Jios, *Spectrochim. Acta, Part A*, 2015, **136**, 1358–1370.
44 V. Y. Sosnovskikh and B. I. Usachev, *Russ. Chem. Bull.*, 2000, **49**, 2074–2076.
45 V. Y. Sosnovskikh and B. I. Usachev, *Russ. Chem. Bull.*, 2001, **50**, 453–455.
46 V. Y. Sosnovskikh and B. I. Usachev, *Russ. Chem. Bull.*, 2002, **51**, 1954–1956.
47 I. C. Henao Castañeda, S. E. Ulic, C. O. Della Védova, N. Metzler-Nolte and J. L. Jios, *Tetrahedron Lett.*, 2011, **52**, 1436–1440.
48 CrysAlisPRO Oxford Diffraction Ltd., Yarnton, England, 2009.
49 G. M. Sheldrick, *SHELXS-86. Program for Crystal Sructure Determination*, University of Göttingen, *Göttingen, Germany*, 1986.
50 G. M. Sheldrick, *SHELXS-97. Program for Crystal Structure Resolution*, University of Göttingen, *Göttingen, Germany*, 1997.
51 L. Farrugia, *J. Appl. Crystallogr.*, 1997, **30**, 565.
52 C. F. Macrae, I. J. Bruno, J. A. Chisholm, P. R. Edgington, P. McCabe, E. Pidcock, L. Rodriguez-Monge, R. Taylor, J. van de Streek and P. A. Wood, *J. Appl. Crystallogr.*, 2008, **41**, 466–470.

53 A. L. Spek, *Acta Crystallogr., Sect. D: Biol. Crystallogr.*, 2009, **65**, 148–155.
54 V. Y. Sosnovskikh, V. S. Moshkin and R. A. Irgashev, *Tetrahedron Lett.*, 2006, **47**, 8543–8546.
55 R. Ballini, L. Barboni and G. Giarlo, *J. Org. Chem.*, 2004, **69**, 6907–6908.
56 P. S. Bevan, G. P. Ellis, H. V. Hudson, T. M. Romney-Alexander and J. M. Williams, *J. Chem. Soc., Perkin Trans. 1*, 1986, 1643–1649.
57 M. J. Frisch, G. W. Trucks, H. B. Schlegel, G. E. Scuseria, M. A. Robb, J. R. Cheeseman, J. A. Montgomery Jr., T. Vreven, K. N. Kudin, J. C. Burant, J. M. Millam, S. S. Iyengar, J. Tomasi, V. Barone, B. Mennucci, M. Cossi, G. Scalmani, N. Rega, G. A. Petersson, H. Nakatsuji, M. Hada, M. Ehara, K. Toyota, R. Fukuda, J. Hasegawa, M. Ishida, T. Nakajima, Y. Honda, O. Kitao, H. Nakai, M. Klene, X. Li, J. E. Knox, H. P. Hratchian, J. B. Cross, C. Adamo, J. Jaramillo, R. Gomperts, R. E. Stratmann, O. Yazyev, A. J. Austin, R. Cammi, C. Pomelli, J. W. Ochterski, P. Y. Ayala, K. Morokuma, G. A. Voth, P. Salvador, J. J. Dannenberg, V. G. Zakrzewski, S. Dapprich, A. D. Daniels, M. C. Strain, O. Farkas, D. K. Malick, A. D. Rabuck, K. Raghavachari, J. B. Foresman, J. V. Ortiz, Q. Cui, A. G. Baboul, S. Clifford, J. Cioslowski, B. B. Stefanov, G. Liu, A. Liashenko, P. Piskorz, I. Komaromi, R. L. Martin, D. J. Fox, T. Keith, M. A. Al-Laham, C. Y. Peng, A. Nanayakkara, M. Challacombe, P. M. W. Gill, B. Johnson, W. Chen, M. W. Wong, C. Gonzalez and J. A. Pople, *Gaussian 03*, Gaussian, Inc., Pittsburgh PA, 2003.
58 R. Ditchfield, *Mol. Phys.*, 1974, **27**, 789–807.
59 I. Dance, *New J. Chem.*, 2003, **27**, 22–27.
60 T. Steiner, *Angew. Chem., Int. Ed.*, 2002, **41**, 48–76.
61 C. B. Aakeroy and K. R. Seddon, *Chem. Soc. Rev.*, 1993, **22**, 397–407.
62 S. Sarkhel and G. R. Desiraju, *Proteins: Struct., Funct., Bioinf.*, 2004, **54**, 247–259.
63 A. Gavezzotti, *J. Phys. Chem. B*, 2003, **107**, 2344–2353.
64 A. Gavezzotti, *J. Phys. Chem. B*, 2002, **106**, 4145–4154.
65 A. Gavezzotti, *Mol. Phys.*, 2008, **106**, 1473–1485.
66 S. Wolff, D. Grimwood, J. McKinnon, M. Turner, D. Jayatilaka and M. Spackman, *CrystalExplorer (Version3.0)*, 2012.
67 D. Jayatilaka, D. J. Grimwood, A. Lee, A. Lemay, A. J. Russel, C. Taylor, S. K. Wolff, P. Cassam-Chenai and A. Whitton, *TONTO – A System for Computational Chemistry*, 2005.
68 R. Dennington, T. Keith and J. Millam, *GaussView, Version 5*, Semichem Inc., Shawnee Mission KS, 2009.
69 O. Trott and A. J. Olson, *J. Comput. Chem.*, 2010, **31**, 455–461.
70 W. Kabsch, *Acta Crystallogr., Sect. A: Cryst. Phys., Diffr., Theor. Gen. Crystallogr.*, 1976, **32**, 922–923.
71 G. R. Desiraju, *Acc. Chem. Res.*, 1996, **29**, 441–449.
72 Y. Ishikawa, *Acta Crystallogr., Sect. E: Crystallogr. Commun.*, 2015, **71**, o495.
73 R. Taylor and O. Kennard, *J. Am. Chem. Soc.*, 1982, **104**, 5063–5070.
74 S. K. Seth, *CrystEngComm*, 2013, **15**, 1772–1781.
75 C. A. Hunter, *Chem. Soc. Rev.*, 1994, **23**, 101–109.
76 T. Dorn, C. Janiak and K. Abu-Shandi, *CrystEngComm*, 2005, **7**, 633–641.
77 M. D. Prasanna and T. N. Guru Row, *CrystEngComm*, 2000, **2**, 134–140.
78 C. Jelsch, K. Ejsmont and L. Huder, *IUCrJ*, 2014, **1**, 119–128.
79 C. Jelsch, S. Soudani and C. Ben Nasr, *IUCrJ*, 2015, **2**, 327–340.
80 C. D. Alcívar León, G. A. Echeverría, O. E. Piro, S. E. Ulic, J. L. Jios, M. Burgos Paci and G. A. Argüello, *Chem. Phys.*, 2016, **472**, 142–155.
81 L. P. Avendaño Jiménez, G. Echeverría, O. E. Piro, S. E. Ulic and J. L. Jios, *J. Phys. Chem. A*, 2013, **117**, 2169–2180.
82 A. Hidalgo, L. P. Avendaño Jiménez, L. A. Ramos, M. A. Mroginski, J. L. Jios, S. E. Ulic, G. A. Echeverría, O. E. Piro and E. Castellano, *J. Phys. Chem. A*, 2012, **116**, 1110–1118.
83 A. C. Neto, L. C. Ducati, R. Rittner, C. F. Tormena, R. H. Contreras and G. Frenking, *J. Chem. Theory Comput.*, 2009, **5**, 2222–2228.
84 J. A. Pereañez, A. C. Patiño, V. Núñez and E. Osorio, *Chem.-Biol. Interact.*, 2014, **220**, 94–101.
85 I. C. Henao Castañeda, J. A. Pereañez and J. L. Jios, *J. Mol. Struct.*, 2012, **1028**, 7–12.

